

PAPER • OPEN ACCESS

Design of a line-of-sight fluorescence-based imaging diagnostic for classification of microbe species

To cite this article: Joshua M Herzog and Volker Sick 2023 *Meas. Sci. Technol.* **34** 095703

View the [article online](#) for updates and enhancements.

You may also like

- [Optical redox ratio differentiates early tissue transformations in DMBA-induced hamster oral carcinogenesis based on autofluorescence spectroscopy coupled with multivariate analysis](#)

R Sethupathi, K Gurushankar and N Krishnakumar

- [Characterization of Hybrid Poly\(acriflavine\)/FAD Films and Their Electrocatalytic Properties with NAD⁺ and NADH](#)

Kuo-Chiang Lin and Shen-Ming Chen

- [Metabolic activity and intracellular pH in induced pluripotent stem cells differentiating in dermal and epidermal directions](#)

Svetlana A Rodimova, Aleksandra V Meleshina, Ekaterina P Kalabusheva et al.

Design of a line-of-sight fluorescence-based imaging diagnostic for classification of microbe species

Joshua M Herzog* and Volker Sick

Department of Mechanical Engineering, University of Michigan, 2350 Hayward St., Ann Arbor, MI 48109, United States of America

E-mail: jmherzog@umich.edu

Received 6 March 2023, revised 26 April 2023

Accepted for publication 19 May 2023

Published 5 June 2023



Abstract

Fluorescence imaging of certain biochemicals, including flavins and pyridine nucleotides, has utility in characterizing the metabolic state of tissue and in discriminating between microbial species. There is significant clinical utility in this class of imaging techniques but most measurements reported to date require specialized training and equipment rendering most implementations unsuitable for routine medical imaging. Here, a low-cost and robust imaging technique is designed using ultraviolet-induced fluorescence of pyridine nucleotides (primarily NADH) and flavins (primarily FAD) in microbial samples. The diagnostic is optimized to distinguish between different microbial species based on previously reported spectral data using a ratiometric imaging approach. A detailed performance analysis is provided that relates the measured fluorescence intensity ratio (FIR) to the relative concentration ratio of NADH to FAD using a simplified spectroscopic model. Analysis suggests the technique is sensitive to changes in the NADH/FAD concentration ratio over several orders of magnitude, with better than 10% FIR precision on a per-pixel basis for microbial smears as thin as 10 s of microns at a resolution of 30 mm^{-1} and exposures of 20 ms. Representative microbe samples from eight species were imaged to demonstrate the proposed technique. Results show that the FIR varies by an order of magnitude across different species but the intra-species variation is only $\sim 5\%$ for the conditions used here. An additional imaging band may be necessary to classify species that contain red pigments or bacteriochlorophyll. Radiative trapping was discussed as a possible limitation of the technique, but no clear evidence for radiative trapping was observed here. Overall, the results suggest that the proposed approach is feasible for rapid, low-cost, and robust characterization of microbial samples.

Keywords: fluorescence imaging, microbe detection, NADH, FAD

(Some figures may appear in colour only in the online journal)

* Author to whom any correspondence should be addressed.



Original Content from this work may be used under the terms of the [Creative Commons Attribution 4.0 licence](#). Any further distribution of this work must maintain attribution to the author(s) and the title of the work, journal citation and DOI.

1. Introduction

Flavin adenine dinucleotide (FAD) and reduced nicotinamide adenine dinucleotide (NADH) play a significant role in cell metabolism and can be probed optically; for this reason they have been targeted in many studies across a variety of cell and tissue types to measure metabolic function and detect various tissue pathologies by taking advantage of the intrinsic fluorescence of NADH and FAD [1, 2]. The NADH to FAD fluorescence ratio in particular, often referred to as the redox ratio, has been used as a general measure of metabolic activity in a variety of applications including cancer tissue analysis [3–9], monitoring wound healing [10–12], and in a variety of other cell metabolism studies [13–17]. Construction of devices for rapid screening or evaluation of samples could provide a robust and cost-effective means for, e.g. pre-clinical drug screening, evaluation of wound or infection healing, detection of surface contamination, diagnosis of cancer, and evaluation of mitochondrial dysfunction.

Similarly, fluorescence spectroscopy using NADH and FAD as probes also have been shown to be promising for the detection and identification of microbe species [18]. Fluorescence intensity and spectra (likely due at least in part to NADH) have been shown to be feasible for evaluating bactericide efficacy [19, 20], and ongoing work is evaluating the use of the redox ratio for identifying bacterial species in urinary tract infections [21]. Other studies have shown promise in discriminating between different bacterial species [22–24] and between bacteria and fungi [25].

Confocal and multiphoton microscopy techniques are often used for fluorescence studies of biological samples in clinical settings because they can be used to construct a three-dimensional fluorescence map with high spatial resolution [26]. Confocal and multiphoton microscopy can achieve high spatial-resolution by using point illumination and exploiting optical nonlinearity, respectively, and multiphoton microscopy in particular can reach penetration depths on the order of 1 mm in biological tissues. However, both techniques can be slow and have limited fields of view resulting from the need to scan the illumination source. There is significant utility in the rapid evaluation of redox ratio or similar measures for the identification of biological cultures and in characterizing tissue samples. However, most quantitative methods reported to date require relatively specialized and expensive equipment, and specialized training. While accurate, these methods can be expensive and inaccessible in many settings, making them largely unsuitable for rapid, low-cost analysis and medical imaging outside of well-equipped laboratories.

Here, a simple, low-cost ratiometric line-of-sight fluorescence imaging technique is developed to distinguish between microbial species based on the results of a previous spectroscopic investigation [27]. In contrast to confocal and multiphoton microscopy, the line-of-sight technique is a two-dimensional path-integrated imaging measurement; the primary benefits are that it is fast, inexpensive, does not require specialized equipment, and is robust since both

fluorescence bands are excited and imaged simultaneously. The shared optical path minimizes bias due to relative motion or differences in source profile and intensity. However, this line-of-sight imaging approach provides only moderate spatial resolution. In the remainder of this report, the proposed technique is analyzed using a combined NADH-FAD fluorescence model and demonstrated on 44 microbial smears across 8 species (non-pathogenic strains of *Bacillus cereus*, *Bacillus subtilis*, *Escherichia coli*, *Micrococcus luteus*, *Pseudomonas fluorescens*, *Serratia marcescens*, and a green bread-mold fungus) to illustrate the utility of the method. This work builds on the previous spectroscopic characterization [27] by developing and demonstrating a novel imaging technique that can be used to distinguish between microbial species.

The diagnostic is designed to target primarily NADH and FAD fluorescence. NADPH, a coenzyme similar to NADH that also plays a role in many metabolic functions, has nearly identical optical properties that make it indistinguishable from NADH [28]. NADPH is likely to be present in samples as well and hence many studies consider NAD(P)H fluorescence, the combination of both NADH and NADPH fluorescence, instead. In the remainder of this article, the label NADH is used exclusively for simplicity. However, it is worth noting that measurements may contain some NADPH fluorescence. Since NADPH and NADH have nearly identical fluorescence properties, the combined NADH-FAD model is believed to be representative of NAD(P)H fluorescence. Several additional biochemicals could be observed with this excitation and collection strategy including collagen [29] and melanins [30, 31]; however, NAD(P)H and FAD are believed to be the dominant source of fluorescence in the samples under consideration here. Other common fluorescent biochemicals including proteins like tryptophan and tyrosine do not fluoresce appreciably at the near-UV excitation wavelengths used here.

2. Methods and materials

A line-of-sight fluorescence-based imaging diagnostic is designed to provide a fast, low-cost, and accessible method for assessing microbial smears; other biological samples including tissue samples are expected to be of interest as well, but are not considered here for simplicity. In principle, the technique is capable of detecting differences between microbe species and metabolic states due to varying concentrations of fluorescent chemicals, primarily NADH and FAD. Other systematic chemical (e.g. production of pigments or solvation effects) and physical differences (e.g. cell size and shape) between species are expected to further alter absorption and fluorescence properties to aid in classification. The proposed technique is a two-color ratiometric fluorescence imaging measurement, which is intended to be the simplest fluorescence diagnostic that retains some spectroscopy information and is conceptually similar to the optical redox ratio. In the remainder of this section, a detailed overview of the technique and design parameters is presented. A methodology for optimizing the collection bands

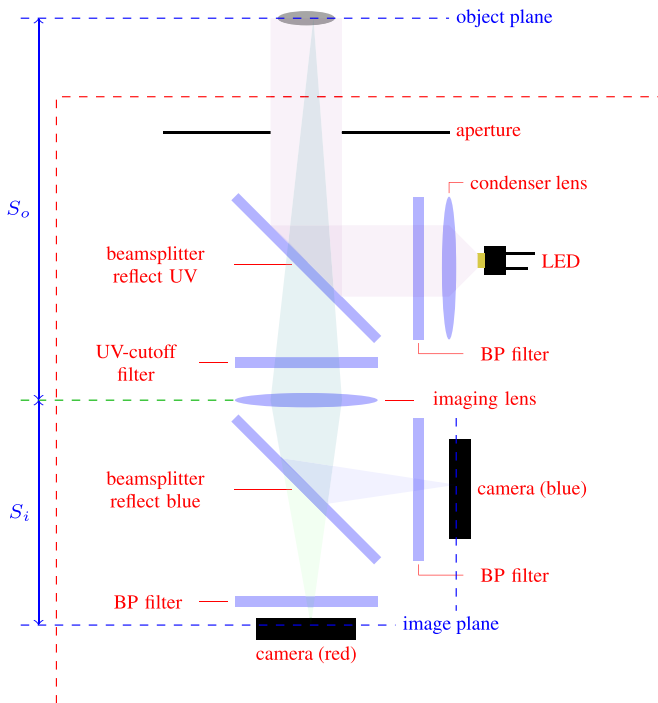


Figure 1. Illustration of device layout with a few key geometric parameters pointed out. The beam path of the excitation source is shaded with violet, while the ray path of the emission from a point on the object plane is shaded with blue and green, respectively.

is presented based on fluorescence data from a small subset of samples. Finally, a combined NADH & FAD fluorescence model is presented which will also be used to analyze the diagnostic performance.

2.1. Overview of technique

The proposed technique is a two-camera, line-of-sight near-UV ratiometric fluorescence imaging tool. A diagram showing the optical layout is provided in figure 1. There are a few interesting features in the proposed design. First, unlike typical ratiometric imaging experiments, the two cameras share an achromatic lens which ensures the image plane distance and camera magnification is fixed between the two cameras. The UV excitation source is placed in front of the imaging lens and provides illumination along the line-of-sight direction. Two dichroic beamsplitters are used in the design; the first is used to direct the UV source towards the object plane while transmitting fluorescence light, and the second is used to separate the fluorescence image between the two image sensors with a cutoff wavelength that is to be determined in this analysis. The fluorescence intensity ratio (FIR) is calculated as the ratio of the two fluorescence images.

Both NADH and FAD can be excited at near-UV wavelengths and have fluorescence quantum yields on the order of several percent in water [32, 33]. NADH and FAD are believed to occur in different concentrations between microbial species in general, and also are known to vary in relative concentration as a function of a cell's metabolic state. Their

utility as a marker for metabolic state has been well established [34]. The diagnostic methodology presented here is optimized to detect differences between measured microbe species, but because the FIR is directly related to the optical redox ratio, the technique is believed to be suitable for detecting metabolic changes in biological samples as well.

2.2. Ratiometric imaging performance

A simplified performance model is used to optimize diagnostic design. For the ratiometric imaging measurement, the measured FIR at each pixel is simply the ratio of the intensity in the red band to that in the blue band, or

$$R = \frac{S_r}{S_b} = \frac{f}{1-f} \quad (1)$$

where S_i is the measured signal in band i , and the subscripts b and r represent the blue and red bands, respectively. On the right-hand side, the FIR is rewritten in terms of the fraction f of the total emission that was captured in band r , and it is assumed that the collection bands are complementary to ensure the maximum signal is collected. For simplicity, the collection bands are assumed to be square, so f is determined only by the cutoff wavelength of the beamsplitter.

The FIR precision is estimated via first-order uncertainty propagation as

$$\left(\frac{s_R}{R}\right)^2 = \left(\frac{s_{S_b}}{S_b}\right)^2 + \left(\frac{s_{S_r}}{S_r}\right)^2 \quad (2)$$

where s_x is the precision index (single-shot standard deviation) in the variable x . For a typical image sensor,

$$s_{S_i}^2 = N_{r,i}^2 + S_i \quad (3)$$

where $N_{r,i}$ is the read noise. In the shot-noise limit, $N_{r,i} \ll S_i$ and $s_{S_i} = \sqrt{S_i}$ such that

$$\left(\frac{s_R}{R}\right)^2 \approx \frac{1}{S_b} + \frac{1}{S_r}. \quad (4)$$

For a total emitted signal $S = S_r + S_b$ with signal-to-noise ratio (SNR) of SNR_0 , the FIR precision can be rewritten as

$$\frac{s_R}{R} = \frac{1}{\sqrt{\text{SNR}_0}} \frac{1}{\sqrt{f-f^2}} = \sqrt{\frac{1+R}{f \text{SNR}_0}}. \quad (5)$$

The FIR precision is clearly optimized when $f = 0.5$, or rather when the signal is split equally between both sensors.

The precision with which relative species concentration can be determined depends on the sensitivity of the FIR to concentration. For a continuous function, e.g. the concentration ratio χ ($\chi = x_{\text{FAD}}/x_{\text{NADH}}$ where x is mole fraction), the measurement precision is given by

$$\frac{s_\chi}{\chi} = \frac{1}{\beta_\chi} \frac{s_R}{R} \quad (6)$$

where β_χ is the dimensionless sensitivity of the FIR to χ :

$$\beta_\chi = \frac{d \log R}{d \log \chi} = \frac{\chi}{R} \frac{dR}{d\chi}. \quad (7)$$

For the discrete case where the FIR is used to identify an organism, the FIR precision is instead compared to the typical variation in FIR between a representative group of species to estimate an error metric as

$$E = \frac{s_R}{\Delta_R} \propto \frac{\sqrt{f}}{\Delta_R(1-f)^{3/2}} \quad (8)$$

where Δ_R is a measure of the variation in FIR between a representative group of samples (e.g. the standard deviation).

The optimum cutoff wavelength is chosen as the value that minimizes the relative error quantity E calculated from measured fluorescence spectra of *E. coli*, *B. subtilis*, and a wild-type green bread mold fungus using data from [27]. Specifically, for each cutoff wavelength, R and s_R are calculated for each spectrum. The standard deviation of R is calculated to estimate Δ_R , and the mean s_R is calculated for comparison with Δ_R . This procedure is repeated for a range of potential cutoff wavelengths, and the cutoff wavelength with the smallest E value is chosen. This procedure effectively calculates the mean FIR precision for each cutoff wavelength and compares it to the variation in FIR across species, and so directly identifies a cutoff wavelength suitable for ratiometric imaging to distinguish between samples.

A second optimization could be performed using the model NADH-FAD spectrum. However, the NADH and FAD models are derived from characterization data of the chemicals in aqueous solution and do not consider changes in the chemical environment or cell morphology between species. In particular, changes in the chemical environment can cause small shifts in absorption and fluorescence feature locations which may be useful in distinguishing bacteria. As such, the measured fluorescence spectra are believed to be a better indicator of changes in microbial fluorescence and are preferred for diagnostic design. The model spectrum instead provides a convenient, species-agnostic tool for performance analysis where the impact of additional parameters including excitation wavelength can be assessed.

2.3. Combined NADH-FAD fluorescence model

A quantitative, combined NADH and FAD fluorescence model is used to analyze the performance of the proposed diagnostic technique. The model is based on aqueous solutions of NADH and FAD (see fit results in [27]), but includes small changes in fit parameters to better match observed *E. coli* spectra which are believed to be representative of NADH and FAD in biological samples. This model provides a convenient method to calculate absorption and fluorescence spectra. The primary limitations of the model are that differences in the chemical environment between microbe samples are neglected, and that cell morphology is ignored. The chemical environment can cause small shifts in absorption and fluorescence features and changes in collisional quenching properties, while cell morphology and inhomogeneity impact radiative transfer and

Table 1. Best-fit values for NADH and FAD using 1D-CCM from [27]. NADH and FAD spectra used for fitting are from [32] and [35, 36]. The FQY (Φ) and radiative deactivation rate (A) for each molecule is included.

	NADH	FAD	units
T''	25 220	20 060	cm^{-1}
ν'	756	775	cm^{-1}
ν'''	818	843	cm^{-1}
δ_q	2.8	2.32	—
W	500	500	cm^{-1}
μ'	3.94	4.32	Debye
μ''	3.63	2.95	Debye
Φ	0.02	0.04	—
A	48.5	17.6	MHz

trapping; both effects are expected to be species dependent¹. However, these simplifications are necessary to provide a useful model for analysis, and are believed to be appropriate for general performance quantification of non-pigmented samples such as *E. coli* and *B. subtilis*.

Mathematically, each molecule is represented by a single one-dimensional configuration coordinate model implemented as a harmonic oscillator. The NADH and FAD absorption and fluorescence spectra are thus each described by a single electronic transition, and absorption and fluorescence spectra are calculated in the Condon approximation. Since FAD has two distinct absorption peaks, likely arising from two electronic transitions, only the longer wavelength peak (near 450 nm) was included in the fit. For shorter wavelength near-UV absorption, experimental data from [35, 36] is interpolated instead and the fluorescence quantum yield (FQY) is assumed to be constant. The model parameters are listed in table 1.

In the Condon approximation, the absorption cross-section and fluorescence rate are given by

$$\sigma(\omega) = \frac{4\pi^2\alpha\omega}{3e^2} |\mu'|^2 \sum_{ij} \frac{e^{-\frac{G'_j}{k_B T}}}{Q'_v(T)} |\langle i|j \rangle|^2 \mathcal{L}(\omega - \omega_{ij}; W) \quad (9)$$

and

$$k(\omega) = \frac{4\omega^3\alpha}{3c^2e^2} |\mu''|^2 \sum_{ij} \frac{e^{-\frac{G''_j}{k_B T}}}{Q''_v(T)} |\langle i|j \rangle|^2 \mathcal{L}(\omega - \omega_{ij}; W) \quad (10)$$

respectively, where ω is the photon angular frequency, α is the fine-structure constant, c is the speed of light, e is the electron charge, μ is the transition dipole moment, G_l is the vibrational energy, k_B is the Boltzmann constant, Q_v is the vibrational partition function, and \mathcal{L} is the lineshape function. Here, the lineshape is assumed to be Gaussian with standard deviation W . The transition frequency between levels i and j in the model is given by

$$\omega_{ij} = T'' + G''_j - G'_i. \quad (11)$$

¹ Thus, the model is not appropriate to describe inter-species variation for, e.g. diagnostic optimization.

where T is the electronic energy; the ground state electronic energy is defined to be zero for simplicity. The superscript prime ('') and double prime ('') are used to indicate the ground and excited states, and $\langle i|j \rangle$ represents the Franck–Condon factor; a harmonic oscillator model is used to simplify the calculation of $\langle i|j \rangle$. Please refer to the appendix of [27] for further mathematical details.

2.4. Imaging demonstration

A ratiometric imaging demonstration was performed for multiple smears from eight different plated microbial cultures. Smears were prepared over the course of two weeks and sampled from different regions to ensure the measurements represent a range of metabolic states. The microbial smears were prepared by streaking approximately 1–3 mm³ of the culture onto a black anodized aluminum substrate and spreading it over a small area with an inoculation loop. The samples were additionally mixed with ~20 µl of distilled water and dried to create a more uniform thickness across the sample. Imaging exposure was varied between 200 and 500 ms to ensure similar imaging precision was achieved with each smear. A series of 10 images was taken and averaged for each sample, and a background correction was performed with the LED turned off using an average over 10 images. A measurement of the LED irradiance profile was made using fluorescence of white paper, and raw signal images were normalized by the LED profile to account for variation in irradiance and collection efficiency (e.g. vignetting). Finally, a mask was generated using an automated threshold technique [37]; regions where the LED irradiance was below 50% of the center value were also masked. Measurements of the cleaned substrate were recorded and showed negligible luminescence intensity.

2.5. Fluorescence spectra

Fluorescence spectra of several microbial samples were measured using a 365 nm LED module (ThorLabs M365LP1) and UV-cutoff filter (ThorLabs FELH0400). Smears were prepared as described in section 2.4. The inoculated substrate was placed approximately 300 mm in front of the focused LED, and was exposed to UV-radiation at approximately 30 mW cm⁻². Fluorescence was collected using a fiber-coupled lens (ThorLabs FMA810-635) placed behind the sample and substrate, and directed into a pocket spectrometer (Ocean Optics USB2000+). The spectrometer was integrated for 20 s and averaged over 30 samples. Measurements were background subtracted and corrected for relative spectral response using a quartz-tungsten halogen lamp (World Precision Instruments, D2H). Spectra were smoothed using a first-order Savitzky–Golay filter with ~10.5 nm window to reduce noise.

3. Results

The optimization procedure was performed to identify the optimum cutoff wavelength based on a limited set of microbe

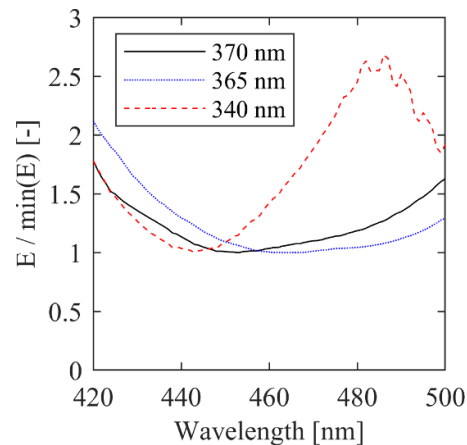


Figure 2. Calculated error metric E as a function of cutoff wavelength for 340, 365, and 370 nm excitation wavelengths.

fluorescence spectra. The optimized collection bands were used to design and assemble an implementation of the diagnostic, and the system was used to image several microbe smears to illustrate the concept. Manufacturer-provided data was used to estimate performance for the diagnostic and performance estimates were made based on the combined NADH–FAD fluorescence model.

3.1. Optimized collection strategy

The calculated error metric is plotted in figure 2 as a function of cutoff wavelength using 340 and 370 nm LEDs (with ~15–20 nm bandwidth) for excitation of *B. subtilis*, *E. coli*, and green bread mold fungus. A third error metric was calculated from spectra acquired here with 365 nm excitation for the seven bacteria species described in section 2.4. The calculation considered only emission from 400 to 530 nm to match the spectra in [27] and to avoid the influence of additional red pigments or fluorophores in the current samples. The error metric was normalized by its minimum value at each excitation wavelength since it does not include absolute fluorescence intensity. From the plot, increasing excitation wavelength from 340 nm increases the optimum cutoff wavelength from 440 to 450–460 nm, consistent with the increase in green fluorescence. Here, the 365 nm LED was chosen for its combination of increased output power and increased green fluorescence compared to the 340 nm LED module, and the optimized cutoff wavelength is ~460 nm.

Band-pass filters were not selected for this application for two reasons. First, stock long- and short-pass filters offer more flexibility in terms of cutoff wavelength selection and can provide transmission bands that are approximately flat with high peak transmission. Stock components are used here exclusively because low-cost and high-availability of optical components is a primary benefit of fluorescence imaging compared to other technologies. Second, the optimal upper cutoff wavelength of the green fluorescence band is not immediately clear from the data presented here; this point will be discussed further in section 4.

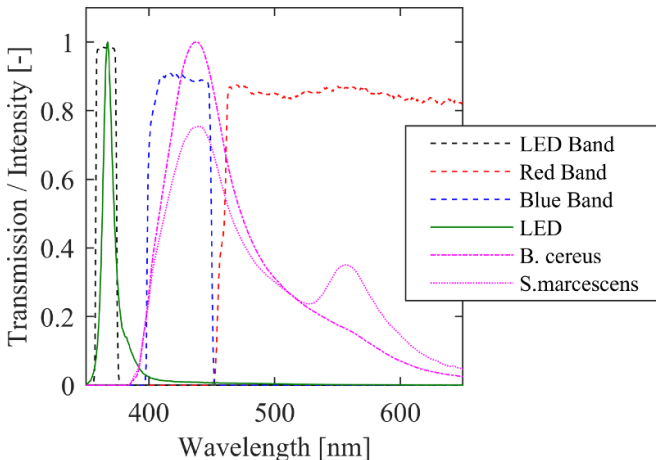


Figure 3. Transmission spectra calculated for the red and blue imaging bands and the LED band based on manufacturer-provided data. The LED emission profile and measured *B. cereus* and *S. marcescens* fluorescence spectra are superimposed.

3.2. Diagnostic implementation

An implementation of the optimized imaging strategy was assembled from stock components. Two identical, 1.6 MP CMOS cameras (ThorLabs CS165MU1) are used to image fluorescence with a 458 nm dichroic beamsplitter (Semrock FF458-Di02). A 365 nm LED with peak power of 2 W is used for excitation (ThorLabs M365LP1), and a 389 nm dichroic beamsplitter (Semrock FF389-Di02) is used to direct the UV emission towards the object plane. The LED emission is restricted with a bandpass filter (Semrock Hg01-365-25). The two image sensors share an achromatic lens (Edmund Optics #65-976) to ensure magnification is consistent between image bands. The LED is focused slightly onto the object plane using a condenser lens (Edmund Optics #48-304). Reflected UV light is rejected using a UV-rejection filter placed in front of the imaging lens (ThorLabs FELH0400). A short-pass filter (ThorLabs FESH0450) and long-pass filter (ThorLabs FELH0450) were used to restrict the collection bands of the blue and red cameras, respectively. The condenser lens and imaging lens were analyzed and selected based on the results of a raytracing calculation.

The transmission bands, calculated from manufacturer-provided data, are shown in figure 3 with the LED emission spectrum and two fluorescence spectra (*B. cereus* and *S. marcescens*) superimposed for reference. The transmission bands for the image sensors include both beamsplitters, the UV-rejection filter, and the long- or short-pass filter as appropriate. The LED band includes the UV beamsplitter and bandpass filter. The camera quantum efficiency is excluded from the plot and is between 50% and 70% in the 400–600 nm wavelength range. Each lens is anti-reflection coated, so losses are typically <0.5% per surface and are excluded from the remaining analysis. Comparing the transmission bands to the fluorescence spectra, the collection bands correlate well with relative changes in fluorescence spectra between species.

An $f/2.0$, 50 mm focal length lens was chosen for the imaging lens and the magnification is chosen to be

Table 2. Performance parameters for proposed implementation. The collection fractions η_x include optical efficiency, filter band transmission, and sensor quantum efficiency.

Symbol	Description	Value	Units
k_f	Fluorescence coeff.	0.05	mm^{-1}
$\eta_{\text{NADH},r}$	NADH red fraction	0.23	—
$\eta_{\text{NADH},b}$	NADH blue fraction	0.26	—
$\eta_{\text{FAD},r}$	FAD red fraction	0.58	—
$\eta_{\text{FAD},b}$	FAD blue fraction	$2 \cdot 10^{-5}$	—
$\eta_{\text{BSub},r}$	<i>B. subtilis</i> red fraction	0.39	—
$\eta_{\text{BSub},b}$	<i>B. subtilis</i> blue fraction	0.14	—
$ M $	Magnification	0.2	—
$f\#$	Lens f -number	2.0	—
$\Omega/4\pi$	Collection fraction	$4.3 \cdot 10^{-4}$	—
l_o	Pixel size	17.25	μm
I'	LED irradiance	30	mW cm^{-2}
N_r	Camera read noise	4.0	e^-
C_{AD}	Analog-to-digital gain	10.74	e^-/ADU

approximately -0.2 . This results in an object plane distance of 300 mm and an approximately 25 mm field of view which is suitable for imaging of samples on, e.g. microscope slides. The object plane pixel size is approximately 17 μm , corresponding to a best-case spatial resolution of $\sim 30 \text{ mm}^{-1}$.

3.3. Performance predictions

Performance factors including collection fraction, the NADH and FAD collection efficiencies per band, the *B. subtilis* fluorescence collection efficiency per band, the excitation irradiance, and the collection volume were calculated and are listed in table 2. A representative fluorescence coefficient for bacterial smears from [27] is included. These parameters are sufficient to estimate performance for imaging of pure NADH-FAD mixtures and for typical bacterial smears assuming the fluorescence spectra are similar to that of *B. subtilis*. The radiometric parameters are used to estimate imaging precision for the model NADH-FAD mixture, and for a representative bacterial smear.

3.3.1. NADH-FAD ratio and sensitivity. The combined NADH-FAD fluorescence model was used to calculate the ratio calibration function R and sensitivity β_χ as a function of excitation wavelength and FAD/NADH concentration ratio χ . The ratio and sensitivity are plotted in figure 4. From the plots, the minimum ratio is approximately 0.8, which is the ratio of pure NADH. As the FAD fraction is increased, $R \propto \chi$ since the vast majority of the FAD emission is captured within the red band. At sufficiently high values of χ , R again approaches a constant value equal to the ratio of pure FAD. The sensitivity over the majority of the plotted range for $\chi > 10^{-1}$ is $\beta_\chi \approx 1$, which is expected for $R \propto \chi$.

At the design wavelength of 370 nm, the measurement is sensitive to χ when $\chi \gtrsim 10^{-1}$. FIRs on the order of 10^2 can be measured with typical image sensors, which suggests that it is feasible to perform this measurement for $10^{-1} \lesssim \chi \lesssim 10^2$ at $\lambda_e \approx 370 \text{ nm}$. Smaller FAD ratios can be measured by

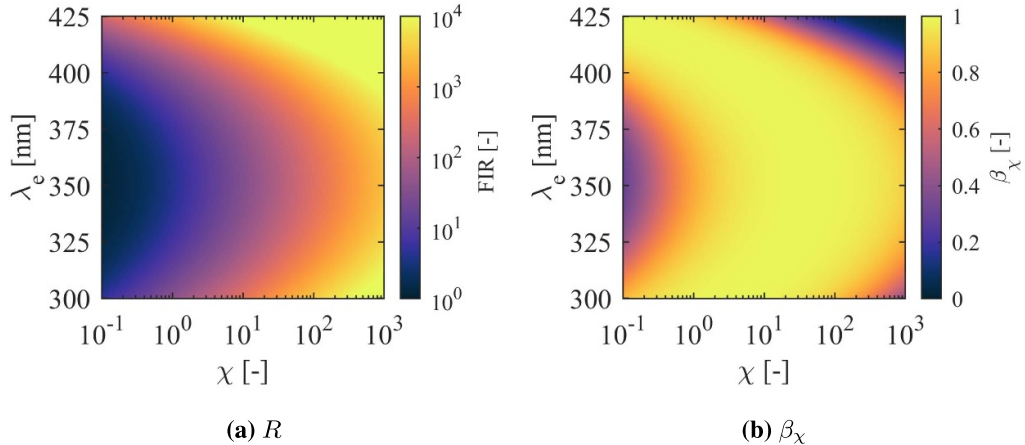


Figure 4. Calculated FIR and sensitivity for NADH-FAD mixture model as a function of excitation wavelength (λ_e) and FAD/NADH concentration ratio (χ).

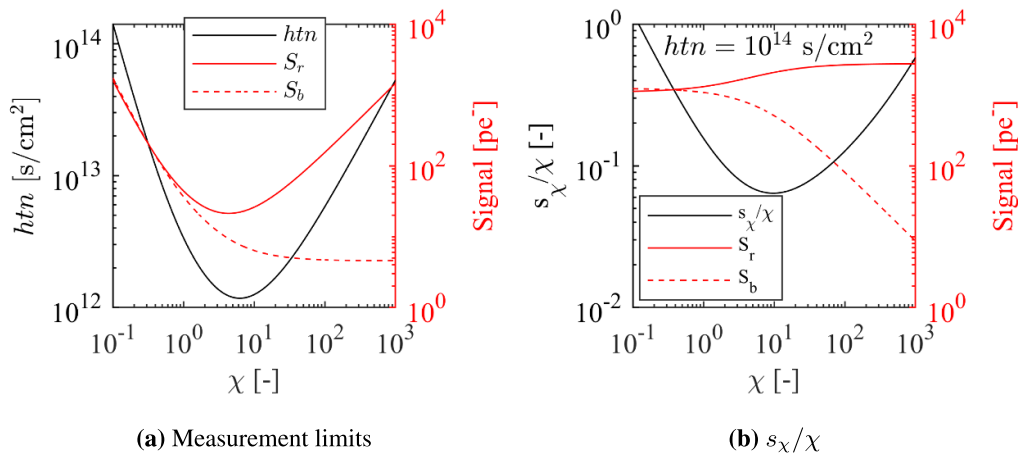


Figure 5. Calculated measurement limits and imaging performance (s_χ/χ for $htn = 10^{14} \text{ s cm}^{-2}$) for mixtures of NADH and FAD.

tweaking the excitation wavelength to preferentially excite FAD more efficiently, e.g. by increasing λ_e ; the dynamic range could also be altered by using different integration durations for each fluorescence band. Notably, the technique is sensitive over approximately 4 orders of magnitude of χ .

3.3.2. NADH-FAD measurement limits. Since the imaging diagnostic provides a line-of-sight measurement, the optical path length or thickness of the sample has a strong impact on imaging performance. Performance also depends strongly on the total concentration of NADH and FAD in the sample. In addition to the concentration ratio χ , performance depends only on the product htn where h is the thickness of the sample, t is the exposure duration, and n is the total number density of NADH and FAD, assuming the sample is thin.

The measurement limit is calculated here as the value of htn as a function of χ such that the SNR of the χ measurement is equal to unity, and the result is plotted in figure 5(a). From the plot, precision is optimized for $\chi \approx 6$, with $htn \approx 10^{12} \text{ s cm}^{-2}$. For a 1 s exposure duration and a 0.1 mm thick sample, this corresponds to a limit of $n \approx 10^{11} \text{ mm}^{-3}$ or a concentration of

$0.2 \mu\text{M}$. The measured signal in electrons is also plotted in the figure; the cameras have a full-well capacity of approximately $11\,000 \text{ e}^-$.

The calculated coefficient of variation (COV) in the measured χ value is plotted in figure 5(b) for a fixed concentration of $htn = 10^{14} \text{ s cm}^{-2}$. For an exposure duration of 1 s and sample thickness of 0.1 mm, this corresponds to $n \approx 10^{13} \text{ mm}^{-3}$ or a $\sim 20 \mu\text{M}$ solution of NADH and FAD. At these conditions, it is estimated that χ can be measured to within 10% per pixel over approximately 2 orders of magnitude. Comparing the signal intensities per channel, the red band actually remains relatively constant and changes by only a factor of ~ 2.5 for any value of χ . The red band intensity is thus a good indicator of total concentration and could be used along with the ratio measurement to provide an absolute concentration measurement for both NADH and FAD.

3.3.3. Signal and ratio precision for microbe film. Performance for the bacterial smear is a function only of the effective film thickness h and integration duration t for a densely packed microbial layer since n is approximately

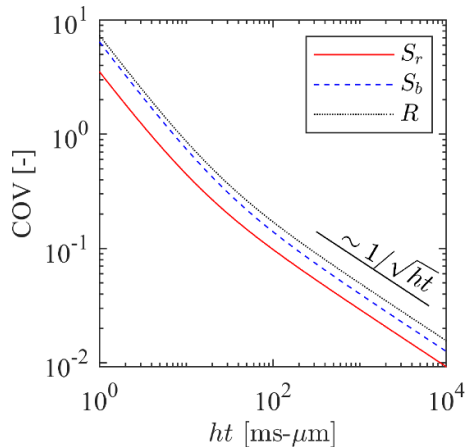


Figure 6. Calculated COV for fluorescence signal and FIR for a *B. subtilis* smear as a function of thickness h and integration duration t using the proposed diagnostic strategy.

fixed by cell geometry. The estimated ratio and fluorescence intensity COVs are plotted as a function of ht in figure 6 for *B. subtilis* assuming a fixed fluorescence coefficient of $k_f = 0.05 \text{ mm}^{-1}$ as reported in [27]. From table 2, the *B. subtilis* FIR is fixed at 1.85, which corresponds to $\chi \approx 0.27$ from the combined NADH-FAD model.

It is clear in the plot that near $ht \approx 30 \text{ ms-}\mu\text{m}$, the measurement becomes shot-noise limited and performance becomes proportional to the square-root of signal intensity; the ratio COV is approximately 0.4 when this occurs. Typical COVs for the FIR for $ht \gtrsim 10^2 \text{ ms-}\mu\text{m}$ are less than 0.2 which suggests that good imaging precision is feasible even for relatively low exposures and thin microbe layers. For example, at a typical thickness of 0.1 mm and exposure duration of 10 ms, $s_R/R \approx 0.05$ with approximately 1000 e⁻ captured in the red band which is well below the saturation threshold. Although the selected cameras are incapable of hardware binning, software binning or averaging could be used to improve measurement precision as needed to determine an aggregate or lower-resolution FIR. An approximate minimum sample thickness for which reasonable quality imaging results can be obtained is 10 μm for a 20 ms exposure, resulting in an FIR COV of ~10%.

3.4. Imaging demonstration

An imaging demonstration was performed on 4–6 samples from each microbial culture over the course of two weeks. The average blue band fluorescence images and FIR images for a representative sample from each culture are shown in figure 7(a), with the measured ratio probability distribution functions (PDFs) plotted in figure 7(b).

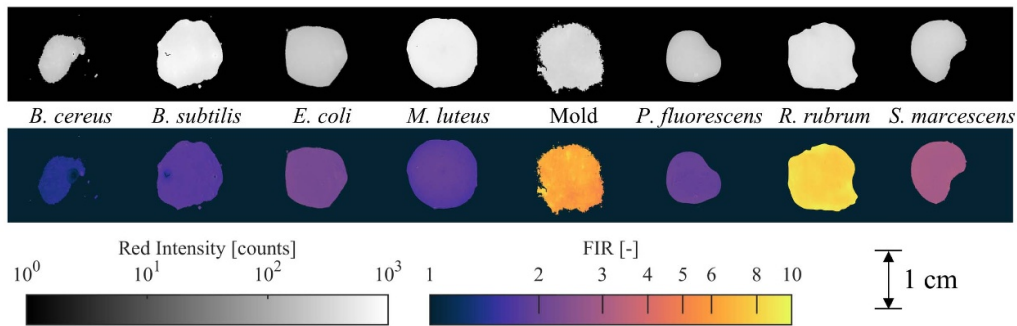
Comparing the FIR PDFs, there is significant variation across species with values ranging from ~1.5 (*B. cereus*) to ~9 (*Rhodospirillum rubrum*). The COV between samples of the same species is on the order of 5% for most species (*B. cereus*, *B. subtilis*, *E. coli*, *M. luteus*, and *P. fluorescens*), while the remaining species have COVs closer to 15%.

Species with higher FIR COVs (*R. rubrum*, *S. marcescens*, and green bread mold) tend to have larger FIR values. This is not surprising as the higher FIR values correspond to weaker blue-band fluorescence intensity, which makes the FIR sensitive to small changes in blue-band fluorescence intensity. It is also possible that the intra-species FIR variation could be influenced by background or stray light where the fluorescence intensity is weak, although there is no clear evidence of this in the data (see figure 7(a) and section 4). Within a given sample, however, the per-pixel variation in FIR is on the order of 10% based on the full-width at half maximum of the distribution functions (corresponding to ~4% standard deviation assuming a normal distribution). The FIR variation within an image is significantly larger than that expected from thermal and shot noise, suggesting that the FIR distributions are dominated by inhomogeneity in the sample.

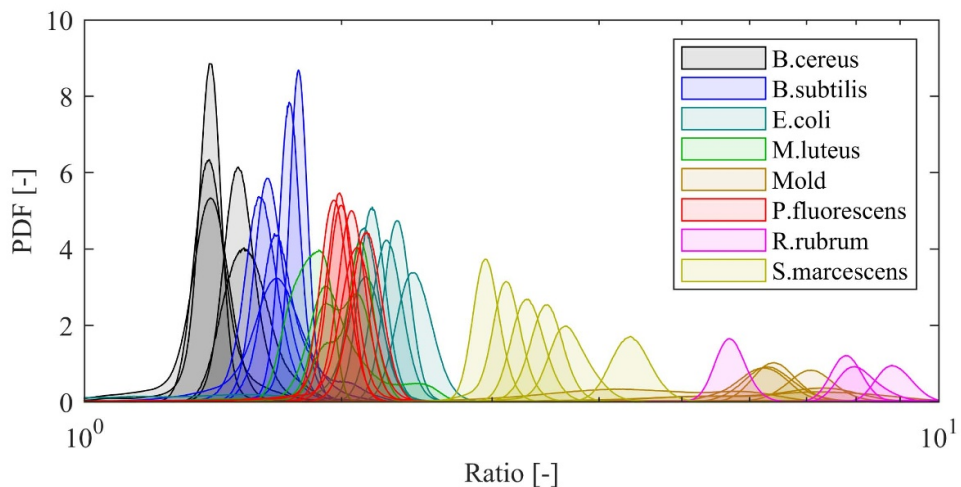
R. rubrum and *S. marcescens* exhibit significantly higher FIR values than the other bacteria samples which is likely influenced by the presence of additional pigments. For example, *S. marcescens* contains the red pigment prodigiosin, the production of which is known to depend on growth phase and available nutrients [38]. Prodigiosin is known to strongly absorb blue and green light and fluoresce at red wavelengths, resulting in an increase in the measured FIR. Likewise, *R. rubrum* produces bacteriochlorophylls and carotenoids when photosynthesis-active and is known to absorb strongly at UV, visible (~590 nm) and infrared wavelengths [39]. Bacteriochlorophyll is also fluorescent and emits between ~750 and 850 nm with a quantum yield on the order of 0.1 [40], which could account for the large FIR and red band emission intensity.

4. Discussion

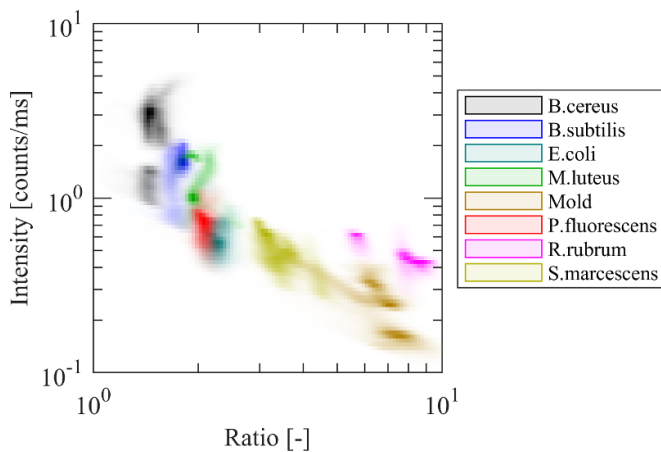
In this manuscript, a detailed design and analysis of an imaging strategy to distinguish between microbial species based on NADH and FAD fluorescence was presented. Performance analysis indicates that even very thin layers can be imaged with good precision, and the technique was demonstrated and data was presented for 44 microbial smears. Since this method uses line-of-sight imaging and excitation, it is possible that radiative trapping could impact the result. Radiative trapping in most bacteria samples here is expected to lead to reduction in blue-band intensity through reabsorption by FAD, increasing the FIR. This would be evident in the data as a dependence of FIR on blue-band intensity within a single sample which is not clearly evident in the data presented here. Joint PDFs of blue-band intensity rate (signal per unit exposure time) and FIR are plotted in figure 8. From the plot, there is an apparent relationship between FIR and blue-band intensity for several samples of *S. marcescens*, *R. rubrum*, and green bread mold fungus; however, because the blue band intensity is so weak for these samples, it is also possible that the observed dependence is a result of a small uncorrected background luminescence from the substrate. Indeed, this possible dependence is apparent only in the samples with the lowest fluorescence



(a) Red fluorescence images (top row) and FIRs (bottom row) for one sample of each species.



(b) Measured FIR PDFs for each sample.

Figure 7. Sample imaging results for 8 species.**Figure 8.** Joint PDF of FIR and corrected blue-band emission intensity rate for each sample.

intensity. On average across all samples tested, the measured FIR is slightly negatively correlated with blue-band intensity within an image ($\langle \rho \rangle \approx -0.2$).

The imaging implementation analyzed here used two imaging bands with a cutoff near 460 nm. However, fluorescence spectra and imaging results suggest there is a significant red

fluorescence component in the pigmented species. The red fluorescence component likely contributes to the increased separation in FIR between the pigmented and non-pigmented bacteria. The addition of a third imaging band for the red fluorescence component could improve classification accuracy, particularly to distinguish between pigmented and unpigmented bacteria. Additional fluorescence spectroscopy investigations are needed to determine appropriate cutoff wavelengths and the impact of a third imaging band on classification accuracy.

5. Conclusion

In this report, an imaging technique was designed to distinguish between microbial species based on the relative concentrations of NADH and FAD using near-UV fluorescence. The method uses ratiometric line-of-sight fluorescence imaging. The collection bands for the diagnostic strategy were chosen based on previously reported fluorescence spectra of several microbial species, and performance estimates for the diagnostic were presented. Measurements of 44 microbial smears across 8 species were presented to demonstrate the technique. A performance model based on NADH and FAD fluorescence was presented and performance estimates were

made. Performance analysis indicates that microbial smears can be imaged with good precision at short exposure durations on the order of 10 ms, and that the FIR measured by the proposed diagnostic is sensitive to the relative FAD fraction over a several orders of magnitude based on the model. Imaging results show that FIR varies predominantly with species, suggesting that the method may be suitable for classifying microbial samples. However, a third imaging band may be necessary to classify species containing red pigments. Radiation trapping was discussed as a potential issue with the measurement, but no clear evidence of this was observed in the imaging data.

Data availability statement

The data that support the findings of this study are openly available at the following URL/DOI: [10.6084/m9.figshare.22194397](https://doi.org/10.6084/m9.figshare.22194397) [41].

Acknowledgments

This work was supported in part by a postdoctoral fellowship funded by the Michigan Economic Development Corporation Technology Transfer Talent Network (T3N) Grant at the University of Michigan. We also would like to thank Rachel Tang and Gianna Agosta for assisting with experiments and data collection.

ORCID iDs

Joshua M Herzog  <https://orcid.org/0000-0001-9089-819X>
Volker Sick  <https://orcid.org/0000-0001-5756-9714>

References

- [1] Datta R, Heaster T M, Sharick J T, Gillette A A and Skala M C 2020 Fluorescence lifetime imaging microscopy: fundamentals and advances in instrumentation, analysis and applications *J. Biomed. Opt.* **25** 071203
- [2] Bartolomé F and Abramov A Y 2015 Measurement of mitochondrial NADH and FAD autofluorescence in live cells *Mitochondrial Medicine* ed V Weissig and M Edeas (New York: Humana Press) pp 263–70
- [3] Alam S R, Wallrabe H, Svindrych Z, Chaudhary A K, Christopher K G, Chandra D and Periasamy A 2017 Investigation of mitochondrial metabolic response to doxorubicin in prostate cancer cells: an NADH, FAD and tryptophan FLIM assay *Sci. Rep.* **7** 1–10
- [4] Liu Q, Grant G, Li S, Wilson C, Li J, Bigner D, Zhang Y, Hu F, Vo-Dinh T and Chen K 2011 Compact point-detection fluorescence spectroscopy system for quantifying intrinsic fluorescence redox ratio in brain cancer diagnostics *J. Biomed. Opt.* **16** 037004
- [5] Lukina M M, Dudenkova V V, Ignatova N I, Druzhkova I N, Lyubov’E S, Zagaynova E V and Shirmanova M V 2018 Metabolic cofactors NAD(P)H and FAD as potential indicators of cancer cell response to chemotherapy with paclitaxel *Biochim. Biophys. Acta* **1862** 1693–700
- [6] Ostrander J H, McMahon C M, Lem S, Millon S R, Brown J Q, Seewaldt V L and Ramanujam N 2010 Optical redox ratio differentiates breast cancer cell lines based on estrogen receptor status *Cancer Res.* **70** 4759–66
- [7] Skala M C, Riching K M, Gendron-Fitzpatrick A, Eickhoff J, Eliceiri K W, White J G and Ramanujam N 2007 *In vivo* multiphoton microscopy of NADH and FAD redox states, fluorescence lifetimes and cellular morphology in precancerous epithelia *Proc. Natl Acad. Sci.* **104** 19494–9
- [8] Wang H-W, Wei Y-H and Guo H-W 2009 Reduced nicotinamide adenine dinucleotide (NADH) fluorescence for the detection of cell death *Anti-Cancer Agents Med. Chem.* **9** 1012–7
- [9] Wu S, Huang Y, Tang Q, Li Z, Horng H, Li J, Wu Z, Chen Y and Li H 2018 Quantitative evaluation of redox ratio and collagen characteristics during breast cancer chemotherapy using two-photon intrinsic imaging *Biomed. Opt. Express* **9** 1375–88
- [10] Jones J D, Ramser H E, Woessner A E and Quinn K P 2018 *In vivo* multiphoton microscopy detects longitudinal metabolic changes associated with delayed skin wound healing *Commun. Biol.* **1** 1–8
- [11] Mokry M, Gál P, Vidinský B, Kušnír J, Dubayová K, Mozeš Š and Sabo J 2006 *In vivo* monitoring the changes of interstitial pH and FAD/NADH ratio by fluorescence spectroscopy in healing skin wounds *Photochem. Photobiol.* **82** 793–7
- [12] Rico-Jimenez J *et al* 2020 Non-invasive monitoring of pharmacodynamics during the skin wound healing process using multimodal optical microscopy *BMJ Open Diabetes Res. Care* **8** e000974
- [13] Hu L, Wang N, Cardona E and Walsh A J 2020 Fluorescence intensity and lifetime redox ratios detect metabolic perturbations in T cells *Biomed. Opt. Express* **11** 5674–88
- [14] Kolenc O I and Quinn K P 2019 Evaluating cell metabolism through autofluorescence imaging of NAD(P)H and FAD *Antioxid. Redox Signal.* **30** 875–89
- [15] Liu Z, Pouli D, Alonso C A, Varone A, Karaliota S, Quinn K P, Münger K, Karalis K P and Georgakoudi I 2018 Mapping metabolic changes by noninvasive, multiparametric, high-resolution imaging using endogenous contrast *Sci. Adv.* **4** ea9302
- [16] Meleshina A V, Dudenkova V V, Bystrova A S, Kuznetsova D S, Shirmanova M V and Zagaynova E V 2017 Two-photon FLIM of NAD(P)H and FAD in mesenchymal stem cells undergoing either osteogenic or chondrogenic differentiation *Stem Cell Res. Ther.* **8** 1–10
- [17] Quinn K P, Sridharan G V, Hayden R S, Kaplan D L, Lee K and Georgakoudi I 2013 Quantitative metabolic imaging using endogenous fluorescence to detect stem cell differentiation *Sci. Rep.* **3** 1–10
- [18] Ammor M S 2007 Recent advances in the use of intrinsic fluorescence for bacterial identification and characterization *J. Fluoresc.* **17** 455–9
- [19] Alimova A, Katz A, Siddique M, Minko G, Savage H E, Shah M K, Rosen R B and Alfano R R 2005 Native fluorescence changes induced by bactericidal agents *IEEE Sens. J.* **5** 704–11
- [20] Li R, Goswami U, King M, Chen J, Cesario T C and Rentzepis P M 2018 *In situ* detection of live-to-dead bacteria ratio after inactivation by means of synchronous fluorescence and PCA *Proc. Natl Acad. Sci.* **115** 668–73
- [21] Sundaramoorthy A, Gnanatheepam E, Purushothaman K, Rao A P, Ganeshan B and Singaravelu G 2021 Discrimination of urinary tract infection bacteria using redox imaging *Multiphoton Microscopy in the Biomedical Sciences XXI* vol 11648, ed A Periasamy, P T C So and K König (California, CA: SPIE) p 116480L

- [22] Dartnell L R, Roberts T A, Moore G, Ward J M and Muller J-P 2013 Fluorescence characterization of clinically-important bacteria *PLoS One* **8** e75270
- [23] Sohn M, Himmelsbach D S, Barton F E and Fedorka-Cray P J 2009 Fluorescence spectroscopy for rapid detection and classification of bacterial pathogens *Appl. Spectrosc.* **63** 1251–5
- [24] Walsh J D *et al* 2013 Rapid intrinsic fluorescence method for direct identification of pathogens in blood cultures *mBio* **4** e00865–13
- [25] Bhatta H, Goldys E M and Learmonth R P 2006 Use of fluorescence spectroscopy to differentiate yeast and bacterial cells *Appl. Microbiol. Biotechnol.* **71** 121–6
- [26] Attia A B E, Bi R, Dev K, Du Y and Olivo M 2020 Clinical noninvasive imaging and spectroscopic tools for dermatological applications: review of recent progress *Transl. Biophoton.* **2** e202000010
- [27] Herzog J M and Sick V 2023 Quantitative spectroscopic characterization of near-UV/visible *E. coli* (pYAC4), *B. subtilis* (PY79) and green bread mold fungus fluorescence for diagnostic applications *J. Fluoresc.* (<https://doi.org/10.1007/s10895-023-03183-6>)
- [28] Blacker T S, Mann Z F, Gale J E, Ziegler M, Bain A J, Szabadkai G and Duchen M R 2014 Separating NADH and NADPH fluorescence in live cells and tissues using FLIM *Nat. Commun.* **5** 1–9
- [29] Menter J M 2006 Temperature dependence of collagen fluorescence *Photochem. Photobiol. Sci.* **5** 403–10
- [30] Kozikowski S, Wolfram L and Alfano R 1984 Fluorescence spectroscopy of eumelanins *IEEE J. Quantum Electron.* **20** 1379–82
- [31] Gallas J M and Eisner M 1987 Fluorescence of melanin-dependence upon excitation wavelength and concentration *Photochem. Photobiol.* **45** 595–600
- [32] Scott T G, Spencer R D, Leonard N J and Weber G 1970 Emission properties of NADH. studies of fluorescence lifetimes and quantum efficiencies of NADH, AcPyADH and simplified synthetic models *J. Am. Chem. Soc.* **92** 687–95
- [33] Islam S D, Susdorf T, Penzkofer A and Hegemann P 2003 Fluorescence quenching of flavin adenine dinucleotide in aqueous solution by pH dependent isomerisation and photo-induced electron transfer *Chem. Phys.* **295** 137–49
- [34] Heikal A A 2010 Intracellular coenzymes as natural biomarkers for metabolic activities and mitochondrial anomalies *Biomark. Med.* **4** 241–63
- [35] Kao Y-T, Saxena C, He T-F, Guo L, Wang L, Sancar A and Zhong D 2008 Ultrafast dynamics of flavins in five redox states *J. Am. Chem. Soc.* **130** 13132–9
- [36] Galbán J, Sanz-Vicente I, Navarro J and De Marcos S 2016 The intrinsic fluorescence of FAD and its application in analytical chemistry: a review *Methods Appl. Fluoresc.* **4** 042005
- [37] Otsu N 1979 A threshold selection method from gray-level histograms *IEEE Trans. Syst. Man Cybern.* **9** 62–66
- [38] Suryawanshi R K, Patil C D, Borase H P, Salunke B K and Patil S V 2014 Studies on production and biological potential of prodigiosin by *Serratia marcescens* *Appl. Biochem. Biotechnol.* **173** 1209–21
- [39] Chang M C, Callahan P M, Parkes-Loach P S, Cotton T M and Loach P A 1990 Spectroscopic characterization of the light-harvesting complex of *Rhodospirillum rubrum* and its structural subunit *Biochemistry* **29** 421–9
- [40] Connolly J S, Samuel E B and Janzen A F 1982 Effects of solvent on the fluorescence properties of bacteriochlorophyll a *Photochem. Photobiol.* **36** 565–74
- [41] Herzog J M and Sick V 2023 Design of a line-of-sight fluorescence-based imaging diagnostic for classification of microbe species *dataset, figshare* (available at: <https://doi.org/10.6084/m9.figshare.22194397>)